COMMUNICATION

ADVANCED MATERIALS
www.advmat.de

Unraveling the Nature of Excellent Potassium Storage in Small-Molecule Se@Peapod-Like N-Doped Carbon Nanofibers

Rui Xu, Yu Yao, Haiyun Wang, Yifei Yuan, Jiawei Wang, Hai Yang, Yu Jiang, Pengcheng Shi, Xiaojun Wu, Zhangquan Peng, Zhong-Shuai Wu, Jun Lu,* and Yan Yu**

The potassium–selenium (K–Se) battery is considered as an alternative solution for stationary energy storage because of abundant resource of K. However, the detailed mechanism of the energy storage process is yet to be unraveled. Herein, the findings in probing the working mechanism of the K-ion storage in Se cathode are reported using both experimental and computational approaches. A flexible K–Se battery is prepared by employing the small-molecule Se embedded in freestanding N -doped porous carbon nanofibers thin film (Se@NPCFs) as cathode. The reaction mechanisms are elucidated by identifying the existence of short-chain molecular Se encapsulated inside the microporous host, which transforms to K$_2$Se by a two-step conversion reaction via an "all-solid-state" electrochemical process in the carbonate electrolyte system. Through the whole reaction, the generation of polyselenides (K$_2$Se$_n$, $3 \le n \le 8$) is effectively suppressed by electrochemical reaction dominated by Se$_2$ molecules, thus significantly enhancing the utilization of Se and effecting the voltage platform of the K–Se battery. This work offers a practical pathway to optimize the K–Se battery performance through structure engineering and manipulation of selenium chemistry for the formation of selective species and reveal its internal reaction mechanism in the carbonate electrolyte.

In-depth understanding on the fundamental mechanism of advanced battery materials is the prerequisite toward efficient material design aiming for property optimization.[1,2] Recently, many efforts have been devoted to developing high-performance K-ion batteries (KIBs) because of abundant potassium resource and lower redox potential of K/K$^+$ than that of Na/Na$^+$, allowing KIBs to be potentially utilized in large-scale energy storage.[3–6] Importantly, the weaker Lewis acidity of K$^+$ which brings about smaller solvated ions as compared to Li$^+$/Na$^+$ could improve diffusion through the electrolyte/electrode interface.[6] Moreover, selenium has emerged as an attractive candidate for KIB cathode thanks to its superior electronic conductivity (10^{-3} S m^{-1})[7] and great electrochemical compatibility with carbonate-based electrolyte[8,9] together with its intrinsically high specific gravimetric capacity (675 mAh g^{-1}) and volumetric capacity (3253 mAh cm^{-3}). Therefore, the K–Se battery, in general, offers higher energy density compared to that based on conventional intercalation cathodes.[10,11] However, its full potential has yet to be unlocked, which is due to the unsatisfactory electrochemical performance arising from dissolution and migration of intermediate polyselenides and large volume expansion during charge/discharge, which are the two typical problems challenging S-based batteries.[12–14] Since the K–Se battery is still at its early stage, there are only very few reports on the cathode development with limited capacity and cycle life,[10,12,15] not to mention largely unknown electrochemical reaction mechanisms involved

---

R. Xu, Dr. Y. Yao, H. Wang, Dr. H. Yang, Dr. Y. Jiang, Dr. P. Shi,
Prof. X. Wu, Prof. Y. Yu
Hefei National Laboratory for Physical Sciences at the Microscale
Department of Materials Science and Engineering
CAS Key Laboratory of Materials for Energy Conversion
University of Science and Technology of China
Hefei, Anhui 230026, China
E-mail: yanyumse@ustc.edu.cn

Dr. Y. Yuan, Dr. J. Lu
Chemical Sciences and Engineering Division
Argonne National Laboratory
205-167A, 9700 South, Cass Ave., Lemont, IL 60439, USA
E-mail: junlu@anl.gov

Dr. J. Wang, Prof. Z. Peng
State Key Laboratory of Electroanalytical Chemistry
Changchun Institute of Applied Chemistry
Chinese Academy of Sciences
Changchun, Jilin 130022, China

Prof. Z.-S. Wu
State Key Laboratory of Catalysis
Dalian Institute of Chemical Physics
Chinese Academy of Sciences
457 Zhongshan Road, Dalian, Liaoning 116023, China
E-mail: wuzs@dicp.ac.cn

Prof. Z.-S. Wu, Prof. Y. Yu
Dalian National Laboratory for Clean Energy (DNL)
Chinese Academy of Sciences (CAS)
Dalian, Liaoning, China

The ORCID identification number(s) for the author(s) of this article can be found under https://doi.org/10.1002/adma.202003879.

DOI: 10.1002/adma.202003879

in this new type of battery. To this end, development of high-performance electrodes and elucidation of their K-ion storage mechanism are of great importance, especially when it comes to the real-time characterization of highly reactive K and those chemically unstable polyselenides as transient intermediates.

In general, the electrochemical performance of a typical battery could be improved by rationally designing new structures and materials that display long cycle life without sacrificing energy density.[16–18] In terms of the K–Se battery, one of such strategies is to construct free-standing carbon–Se composited thin-film electrode, which in theory could achieve high Se loading with high energy density. This design will also eliminate the use of electrochemically inactive binders and current collector[19] and simplify the investigation of underline mechanisms of the active materials involving in the electrochemical reactions without being affected by any inactive ingredients. 1D nitrogen-doped carbon nanofibers are particularly attractive in the search of ideal hosts that can strongly combine with Se due to their abundant active sites for ion storage, high electronegativity, excellent mechanical and chemical stability.[17,19,20] One can reasonably expect that the integration of the above strategies can greatly enhance the K-ion storage performance. However, it remains a great challenge to develop a facile process to fabricate such composite electrode.

Inspired by the advantageous structure of peapod, we design a film-like KIB cathode by employing freestanding small-molecule Se@peapod-like N-doped porous carbon nanofibers (denoted as Se@NPCFs) to achieve enhanced performance for K–Se batteries. The unique structure of the composite electrode features several advantages. First, 1D peapod-like structure with periodic macropores in the fibers facilitates the electrolyte infiltration and K^+ diffusion, and therefore alleviates the concentration polarization.[21] Second, the abundant micro/mesopores enable increased mass loading of Se, shorten the ion diffusion distance and buffer the volume expansion. Third, N-doping greatly enhances the chemical affinity between the carbon matrix and discharge products,[22,23] supported by our density functional theory (DFT) calculation. Lastly, the 3D interconnected conductive framework of Se@NPCFs could decrease the resistance of ion and electron diffusion during charge/discharge, leading to enhanced high-rate capacity.[24] Taking all these advantages together, our Se@NPCFs deliver unprecedented cycling stability (367 mAh g^{-1} after 1670 cycles at 0.5 A g^{-1}), and even shows superior mechanical flexibility. We also dig deep into the reaction mechanisms of K–Se chemistry using operando Raman spectroscopy, ex situ high-resolution TEM (HRTEM), first-principle calculation and time-of-flight secondary-ion mass spectrometry, which suggests an "all-solid-state" electrochemical reaction mechanism proceeding via a two-step conversion reaction. The results demonstrate that Se confined in the host majorly presents in the form of small and short-chained molecules, which, upon K^+ insertion, circumvents the formation of polyselenides (K_2Se_n, $3 \leq n \leq 8$) and transforms to K_2Se via forming solid K_2Se_2 as the intermediate product. The notorious polyselenides are thus effectively suppressed by electrochemical reaction dominated by Se_2 molecules, thus significantly enhancing the utilization of Se which accounts for the superior energy storage performance of K–Se batteries.

Figure 1a shows the fabrication process of the Se@NPCFs film electrode via electrospinning. In a typical procedure, the

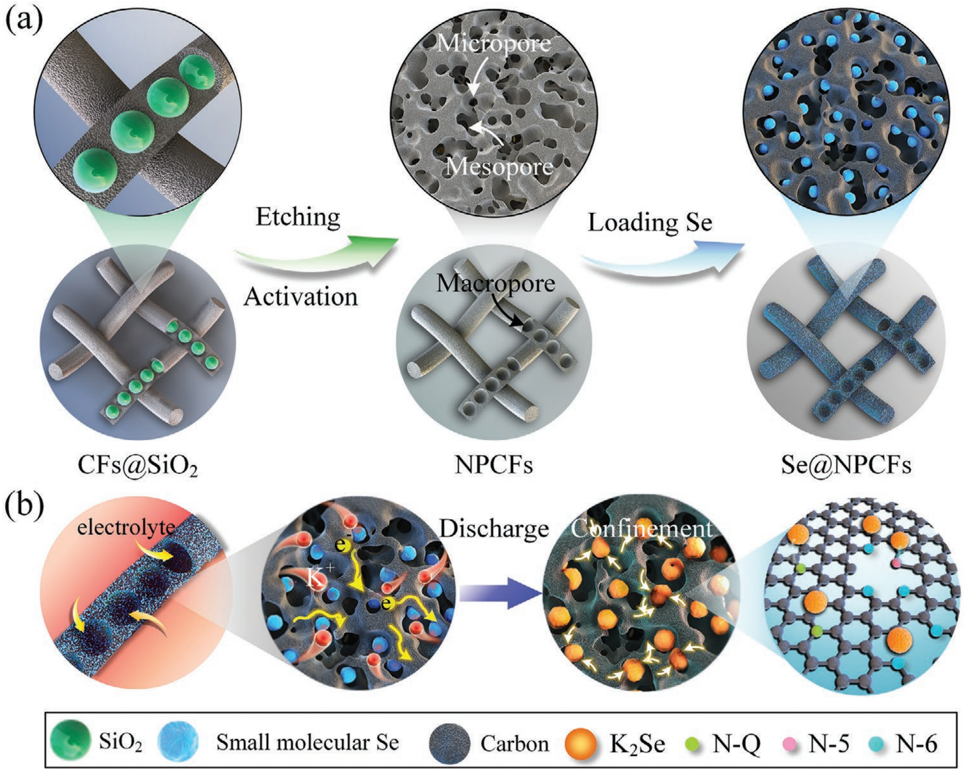

Figure 1. Schematic diagram of design idea and synthesis process. a) Schematic diagram of the preparation process for the Se@NPCFs composite electrode. b) Illustration of the advantage of the nitrogen-doped Se@NPCFs composite with abundant micropores during the potassiation process.

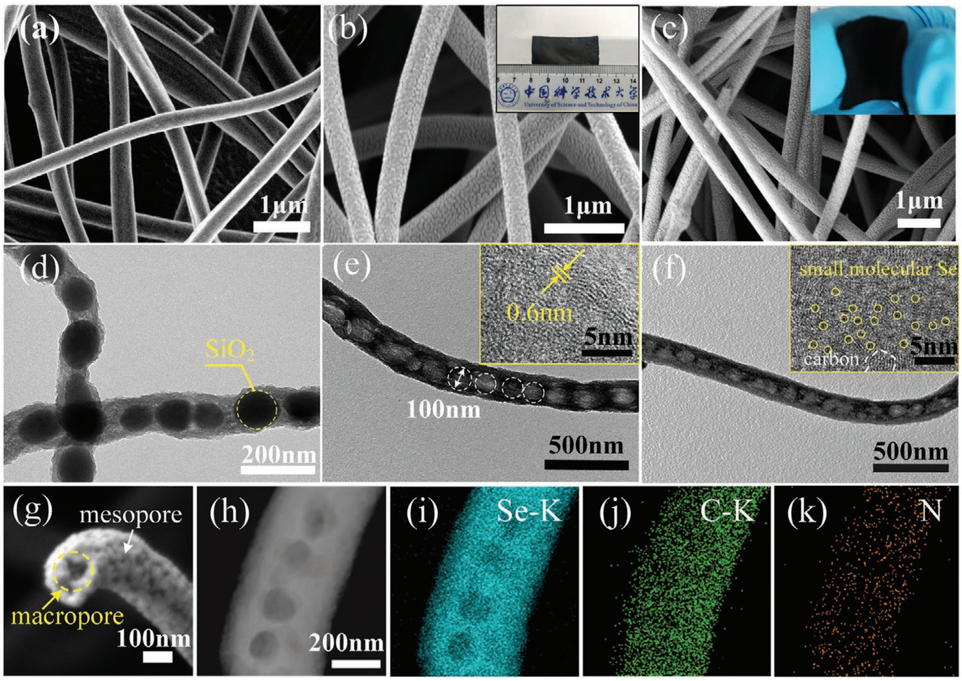

Figure 2. Morphology and structure characterizations of Se@NPCFs. a–c) SEM images of SiO_2@CFs (a), NPCFs (b), Se@NPCFs (c); The insets in (b) and (c) show the photograph of freestanding NPCFs and flexible Se@NPCFs films respectively. d–f) TEM images of SiO_2@CFs (d), NPCFs (e), Se@NPCFs (f); The insets in (e) and (f) show high-resolution TEM images of NPCFs and Se@NPCFs, respectively. g) SEM image of cross-section of one Se@NPCF. h–k) The dark-field TEM image of Se@NPCFs, and corresponding EDS mapping of K (i), C (j), and N (k).

precursor solution of polyacrylonitrile (PAN), triblock copolymer Pluronic F127, and tetraethylorthosilicate (TEOS) in *N*, *N*-dimethylformamide (DMF) was electrospun into a membrane of nanofibers.[25–27] Subsequently, the as-prepared nanofibers were carbonized in Ar/H_2 atmosphere at 1200 °C, leading to the formation of SiO_2@carbon nanofibers (SiO_2@CFs) thin film. After removing the SiO_2 nanoparticles from the SiO_2@CFs fibers by diluted HF solution, a unique peapod-like morphology with abundant pores (NPCFs) was obtained through an activation process using KOH solution and NH_3. Finally, Se was infiltrated into the NPCFs by molten liquefaction strategy without destroying the initial freestanding and flexible thin-film electrode (Se@NPCFs). Such a 3D interconnected porous conductive structure with N-doping not only facilitates the K-ion diffusion and electron transfer, but also buffers the large volume expansion during charge/discharge process, which guarantees decent cycling stability and high capacity of the electrode, as schematically illustrated in Figure 1b. For comparison, the electrode with the same loading amount of Se but without the NH_3 activation step was also prepared (denoted as Se@CFs).

The morphological evolution of the samples was monitored by the field-emission scanning electron microscopy (FESEM). As shown in Figure S1a, Supporting Information, the as-prepared PAN/F127/TEOS nanofibers show an average diameter of about 300 nm. SiO_2 clusters are uniformly dispersed within the fibers (Figure S1b, Supporting Information). After heat treatment in Ar/H_2, the morphology of the SiO_2@CFs remains intact (**Figure 2**a). The surface of the NPCFs becomes rougher as the result of pore formation after subsequent etching and activation processes (Figure 2b). The interconnection of 1D macroporous nanofibers constructs a 3D interlinked conductive network, which is beneficial for enhancing the penetration of electrolyte and electron/ion transport. After the infiltration of Se, the morphology and structure of the obtained Se@NPCFs film are highly resemble to the NPCFs, along with the excellent mechanical flexibility inherited from the carbon skeleton (Figure 2c). The Se@NPCFs can be bent into curved structure (inset in Figure 2c). Transmission electron microscopy (TEM) was also conducted to trace the structural evolution of the samples. Figure 2d reveals that SiO_2 spherical particles are uniformly embedded in the nanofiber, which is driven by the tendency of small SiO_2 clusters to undergo inward transfer and aggregate at high temperature.[24] After the etching process, ordered macropores (about 100 nm) are evenly created along the axial direction of the nanofiber (Figure 2e). HRTEM imaging (inset in Figure 2e) further reveals that the shells of these peapod-like nanofibers contain plenty of micro/mesopores, leading to uniform encapsulation of Se with high mass loading in the subsequent step.[28] Ordered macropore structure of the composites is manifested in Figure 2f, indicating that Se was filled preferentially into the micro/mesopores of the NCPFs via capillary force action.[29] The circled darker region in the inset of Figure 2f confirms the existence of small-molecular Se while the cross-sectional view of Se@NPCFs displays an open porous structure with different porosity (Figure 2g). The dark-field TEM image and EDS elemental mappings of the Se@NPCFs were shown in Figure 2h–k, demonstrating homogeneous distribution of Se, C, and N species in the Se@NPCFs. For comparison, the Se@CFs exhibit similar structure to Se@NPCFs (Figure S1c, Supporting Information) also presenting an amorphous nature of Se (Figure S1d, Supporting Information). Clearly, the above fabrication process allows the infiltration of Se molecules into the inner void space of peapod-like nanofibers through the micro/mesopores on the shell during the molten liquefaction process.[30] Consequently, such confined molecular Se can be utilized without unfavorable transition to high-order polyselenides caused by bulky Se during cell discharge.[31] In addition, the partially filled micro/mesopores could also alleviate the volume expansion effectively.

The structure of the NPCFs, commercial Se powder and Se@NPCFs were investigated by X-ray diffraction (XRD) (Figure S2, Supporting Information). The NPCFs show a broad diffraction peak located at around 25°, corresponding to the (002) plane of amorphous carbon. For the commercial Se powder, the diffraction pattern corresponds well with the trigonal Se comprising infinite helical Se chains (JCPDS card No. 86–2246). On the other hand, the Se@NPCFs display amorphous characteristic without showing any signal of Se, indicating complete infiltration of small-molecular Se into porous carbon skeleton, which is in accordance with our HRTEM observation. Raman spectroscopy of the Se@NPCFs (Figure S3, Supporting Information) shows a sharp peak at 237 cm^{-1} arisen from the intrachain stretching vibration mode of Se powders. In addition, a blueshift to 251 cm^{-1} corresponds to the characteristic peak of amorphous Se.[32] This can be attributed to structural transformation from helical Se chains to polymeric Se chains induced by melt-infiltration. It is worth noting that amorphous Se was claimed to be exclusively composed of Se chains instead of Se_8 rings by $_{77}Se$ NMR spectroscopy in a recent study,[32] unlike the sulfur with cyclic structure (cyclo-S_8). Two peaks located at 1353 cm^{-1} (D band) and 1595 cm^{-1} (G band) can be assigned to disordered sp^3 graphite and sp^2 hybridized carbon atoms, respectively.[33]

X-ray photoelectron spectroscopy (XPS) was applied to investigate the surface species of the Se@NPCFs. Figure S4, Supporting Information confirms the existence of C, N, Se, and O elements in the Se@NPCFs. C1s spectra was fitted into four peaks located at 284.6, 285.1, 286.7, and 288.6 eV, corresponding to the C—C, C—O, C—N, and O=C—O bonds, respectively. Four types of N species shown in N1s spectra are pyridinic N (398.5 eV), pyrrolic N (399.9 eV), quaternary N (402.8eV), and N–Se bond (408.5 eV).[33] In terms of N-Q, N-5, and N-6 three different nitrogen doping positions, the content of N-6 in the Se@NPCFs is up to 46.8 wt% which owns the highest ratio, while the content of N-5 and N-Q are only 29.3 and 23.9 wt% respectively (Table S1, Supporting Information). Studies have shown that rich N-5 and N-6 could offer more favorable electron transfer between K^+ and C/Se composites compared to N-Q, leading to enhanced electrochemical performance.[15,33] Additionally, Se 3d spectra can be deconvoluted into three different peaks, which are Se $3d_{5/2}$ (55.5 eV), Se $3d_{3/2}$ (56.2 eV) due to a spin-orbit interaction and Se–O (59.0 eV).[34] The N atomic percent of the Se@NPCFs reaches up to 5.14 at%, whereas only 0.93 at% is observed in the Se@CFs. The high N-doping signifies that the N heteroatoms were successfully doped in the carbon nanofiber during NH_3 activation. The increasing amount of nitrogen induces plenty of internal defects and active sites, thus providing intimate contact between small Se molecules and carbon matrix.[35]

N_2 adsorption and desorption isotherm measurement was performed to investigate the specific surface areas of the CFs and NPCFs (Figure S5, Supporting Information). A type-III isotherm with a high nitrogen uptake at low relative pressure and a hysteresis loop at high relative pressure are attributed to the highly porous structure of the NPCFs.[36] The BET surface area of the NPCFs (789 $m^2 g^{-1}$) is significantly higher than that of CFs (153 $m^2 g^{-1}$), indicating that NH_3 activation generates a large amount of pores in NPCFs.[37] According to the thermogravimetric analysis (TGA) (Figure S6, Supporting Information), Se content in Se@NPCFs is estimated to be 62 wt%, which is the highest Se-loading value among all reported Se/C composites for K–Se batteries. The reduced specific surface area (15 $m^2 g^{-1}$) and pore size distribution of the Se@NPCFs (Figure S7, Supporting Information) further suggest that Se is fully permeated into the micro/mesopores of the NPCFs thin film. For comparison, similar amount of Se is also loaded to CFs.

Electrochemical properties were evaluated by assembling CR2032 coin cell. The coin cell that used the Se@NPCFs film as cathode and metal K as anode was evaluated in carbonate electrolyte (EC (ethylene carbonate)/DEC (diethyl carbonate)) in the voltage range of 0.5–3.0 V (versus K^+/K). The specific capacity was calculated based on the mass of active material, Se. From the voltage profile (**Figure 3**a), the highly stable capacity was preceded by an exceedingly large but irreversible capacity in the first cycle (1045 and 631 mAh g^{-1} upon discharge and charge respectively). The low initial Columbic efficiency could be attributed to the solid electrolyte interface (SEI) layer formation and electrolyte decomposition. Furthermore, the voltage dip that plunged to a lower potential plateau in the first cycle indicates impeded transport of K ions that is conceivably linked to the deformation of ion solvation shell to accommodate the extremely small pore size before they successfully diffused into the microspores. In the following cycles, two flat discharge plateaus (around 1.45 and 1.20 V) were observed, which were consistent with the cyclic voltammograms (CV) curves. The similar galvanostatic discharge/charge profile of the 50th cycle indicated the good electrochemical reversibility and cycling stability of the Se@NPCFs. At low current density of 50 mA g^{-1}, Se@NPCFs displayed a stable capacity of 635 mAh g^{-1} with 98.1% Columbic efficiency over 50 cycles (Figure 3b), indicating an outstanding utilization rate (94.1%) of active Se (the theoretical capacity of Se is 675 mAh g^{-1}). In contrast, Se@CFs only delivered a low discharge capacity of 445 mAh g^{-1} with 66% of Se utilized and the initial Columbic efficiency is very low (38.8%). Besides, the Se@NPCFs delivered remarkable rate performance that achieved 611, 554, 450, 355, and 209 mAh g^{-1} at 0.1, 0.2, 0.5, 1.0, and 2.0 A g^{-1}, respectively (Figure 3c). When the current density was switched back to 0.1 A g^{-1}, an average reversible capacity of 578 mAh g^{-1} could still be obtained (capacity retention: 95%). More impressively, the Se@NPCFs presented a high capacity retention of 367 mAh g^{-1} after ultralong cycling over 1670 cycles with nearly 100% Columbic efficiency at a current density of 0.5 A g^{-1} (Figure 3d). To the best of our knowledge, the long-term cycle life and high reversible capacity of the Se@NPCFs reported here are unprecedented for K–Se batteries (Table S2, Supporting Information).[12,13,15] To demonstrate the practical application of Se@NPCFs electrode for KIBs, a pouch cell that used K metal as anode was assembled. The pouch cell managed to light up a red

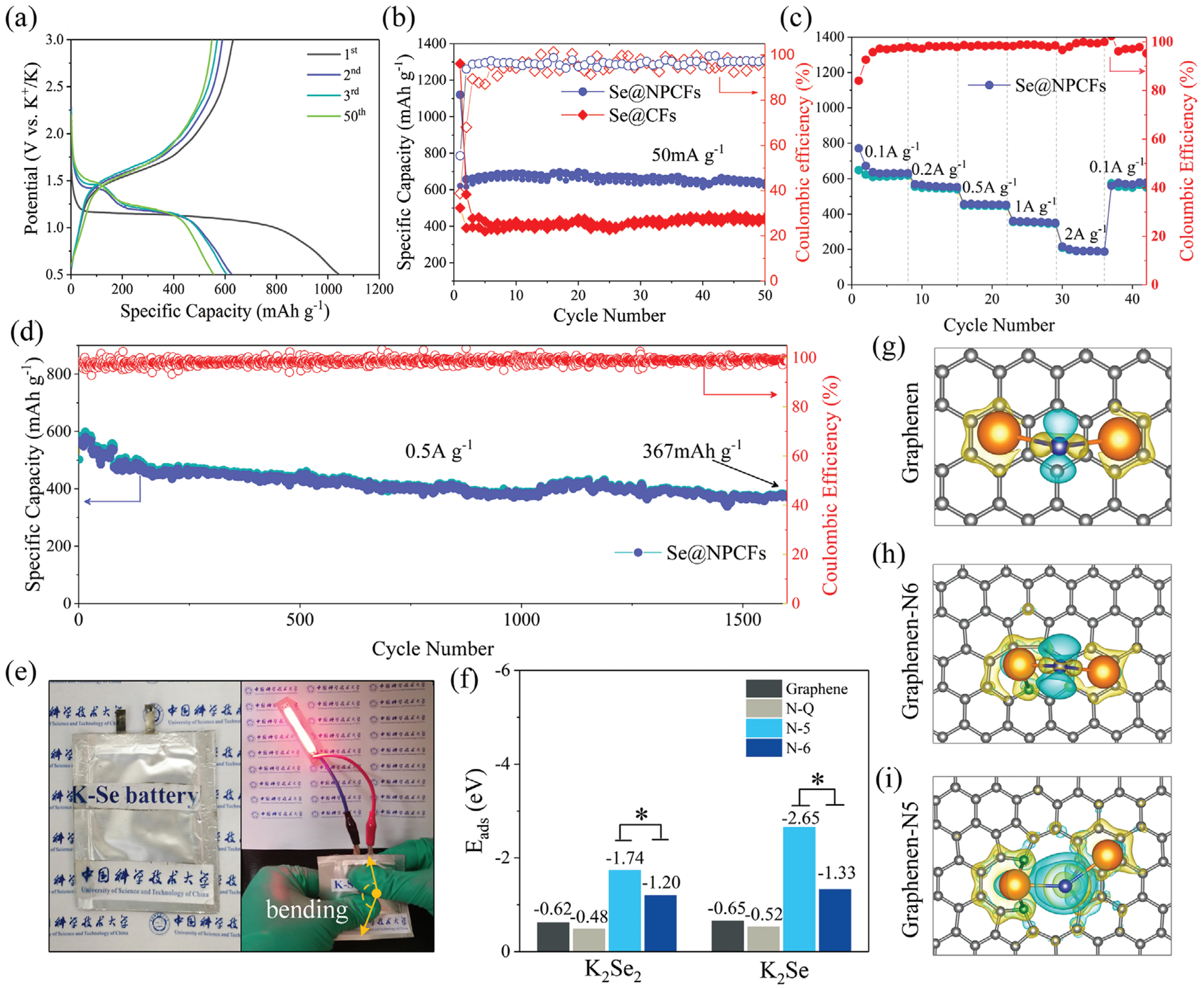

Figure 3. Electrochemical properties of Se@NPCFs and corresponding theoretical simulations. a) The galvanostatic charge and discharge profiles at various cycles of the Se@NPCFs at 0.1 A g^{-1} (0.7 м KPF6, EC: DEC). b) Cycling performance of the Se@CFs and Se@NPCFs at small current density of 50 mA g^{-1}. c–d) Rate performance and prolonged cyclability at 0.5 A g^{-1} for the Se@NPCFs. e) The soft packing of a K–Se full battery. f) The corresponding adsorption energy of K_2Se and K_2Se_2 adsorbed in the N-5, N-6, N-Q, and graphene structures. g–i) Electron density differences of K_2Se absorbed in the graphene (g), N-6 (h), and N-5 (i) structures. The yellow and turquoise areas represent increased and decreased electron density, respectively. The isosurfaces are the 0.001e $bohr^{-3}$. Silver, green, purple, and orange balls represent carbon, nitrogen, potassium and selenium atoms, respectively.

light-emitting diode (Figure 3e) and continued to function as normal without structural failure even under dynamic bending (180°) for repeated cycles, indicative of excellent mechanical flexibility and structural stability of the electrode (see the Video in the Supporting Information). The enhanced performance could be attributed to the synergistic effect of the geometrical and structural design of the Se@NPCFs. First, the small-molecular Se can bypass the formation of polyselenides that lead to a cascade of undesired side reactions. Second, the confinement of Se molecules in well-design pore structure can effectively accommodate huge volume change during cycling. Third, the 3D interconnected carbon nanofibers provide interlinked pathways for electron conduction. Finally, the highly porous structure guarantees continuous supply of K^+ for the embedded Se, which greatly improves the reaction kinetics of the electrode.

To further elucidate the experimental results, we conducted a theoretical investigation of the adsorption ability of the NPCFs for discharge products (K_2Se_2: Crystallography Open Database Card No: 96-901-1377 and K_2Se: JCPDs Card No: 77–2153). The discharge products will be discussed in the mechanism section in detail. In our simulation model, N-5, N-6, N-Q, and undoped-N graphene were employed to examine the adsorption ability towards K_2Se_2 and K_2Se (Figure S8, Supporting Information). Based on the results (Figure 3f), the adsorption energy of N-5 and N-6 for K_2Se_2 are –1.74 and –1.20 eV, respectively, much higher than those of the N-Q (–0.48 eV) and graphene (–0.62 eV). Correspondingly, the N-5 and N-6 exhibit higher adsorption energy (–2.65 and –1.33 eV) for K_2Se as well, which are comparable to those of N-Q (–0.52 eV) and graphene (–0.65 eV). It is suggested that the affinity of the N-5 and N-6 to

K_2Se/K_2Se_2 is more prominent than those of the graphene and N-Q. For Se@NPCFs, high level of N-doping could enhance its chemical anchoring effect on discharge products K_2Se_2/K_2Se to minimize their detachment from the pores of carbon matrix during cycling.

The electronic charge density of the K_2Se molecule on three different substrates upon adsorption is shown in Figure 3g–i. A reduced charge density around the Se atom along with an increase in charge density on the substrate indicates that the electron transfer from K_2Se molecule to substrate upon absorption is energetically favorable. Furthermore, the charge shows higher tendency to flow from Se to N-doped substrate compared with undoped substrate, which indicates that penta-coordinate N can significantly enhance the affinity between K_2Se molecule and substrate. These findings further validate our hypothesis that the improved properties of the NPCFs stem from the enhanced charge transfer between the N-doped graphene and K_2Se.

The reaction kinetic of the Se@NPCFs was further analyzed by CV measurement at different scan rates (Figure S9, Supporting Information). It could be observed that the polarization voltage increases with the increasing of scan rate. The current changes with regard to the scan rate could be expressed by the following equation:

$$\log(i) = \log(a) + b\log(v) \tag{1}$$

where i is the peak current, v is the scan rate, a and b are the fitting constants. The reaction kinetics can be mathematically analyzed by comparing the b values of various groups. In particular, the closer to 1 that b is, the more prominent capacitive-dominant energy storage the material possesses, which contributes to faster kinetics.[38] The fitting curve in Figure S10, Supporting Information shows an almost linear relationship, and the b value of cathodic peaks and anodic peaks are calculated to be 0.84 and 0.74, respectively, with an almost liner relationship.

To study the mechanistic details of the Se@NPCFs, CV measurement was carried out in EC/DEC electrolyte in the voltage window of 0.5–3.0 V (versus K^+/K) at a scan rate of 0.2 mV s^{-1} (Figure S11, Supporting Information). In the cathodic scan, only one reduction peak at 0.7 V was observed in the first cycle, suggestive of a one-step reaction. However, a couple of cathodic peaks emerged in the second cycle within the voltage range of 0.90–1.28 V, which is indicative of a different electrochemical behavior compared with the initial cycle. The slight shift in cathodic peaks to higher potential of 1.10 and 1.41 V in the following cycles could be possibly caused by electrochemical activation or the stabilization process of the chain-like Se molecules.[39] The almost overlapped anodic and corresponding cathodic peaks in the subsequent cycles are an indication of the highly reversible reaction in the electrode. To gain insight into the structural and compositional evolution of the Se@NPCFs electrode, in situ Raman spectroscopy and ex situ HRTEM were carried out to characterize the changes in electrode during the initial CV measurement and the second discharge/charge cycle (at 100 mA g^{-1}), respectively. As illustrated in **Figure 4**a, the typical trigonal Se characteristic peak gradually vanished upon discharging to 0.77 V. Simultaneously, the broader amorphous Se peak (254 cm^{-1}) due to polymeric Se chains[40] shifted slightly to 252 cm^{-1} (Figure S12, Supporting Information) and became more intense as the reaction progressed, which is the result of the electrochemical reduction of the Se chains. Another two discernible peaks at around 147 and 212 cm^{-1} strikingly appeared. At the fully discharged state (0.5 V), the above three vibrational adsorption peaks were still shown. When the cell was charged in the reverse process, all of peaks began to fade out; meanwhile, the peak of 254 cm^{-1} started to occur at 0.5 and the intensity gradually increased until 3.0 V, indicating that the discharge product was reoxidized into the chain-like Se molecules.

Previous research on Li–S batteries in carbonate electrolyte system has confirmed the direct conversion of cyclo-S_8 to Li_2S.[41,42] The chemical similarity between S and Se prompts us to propose similar mechanism in the K–Se system. Based on our speculation, the unidentified signals in the discharge process could possibly be K_2Se. Hence, K_2Se powder was intentionally synthesized as a reference in the comparative study (Figure S13, Supporting Information).[43] The XRD pattern of as-synthetized K_2Se powder (Figure S14, Supporting Information) can be indexed to K_2Se[44] and residual naphthalene. The obtained Raman peaks of the K_2Se at 147, 212, and 252cm^{-1} were near-perfectly consistent with the in situ Raman results (Figure S15, Supporting Information), which validated the aforementioned conjecture and ruled out the effects of naphthalene. Clearly, no existence of linear polyselenides was observed, confirming that the Se@NPCFs cathode undergoes solid-state reaction without the generation of any other intermediate polyselenides in the initial discharge cycle in carbonate electrolyte. Figure 4b shows a 2D contour plot of the Se@NPCFs Raman spectra during the cathodic scan, suggesting that the transition from chain-like Se molecules to K_2Se takes place in a gradual manner. It is noteworthy that the initial phase of trigonal Se (237 cm^{-1}) is hardly recoverable, which is largely due to the higher electrochemical reactivity of the amorphous Se in metastable state that endows it with higher surface-to-bulk ratio and dangling bonds than its crystalline counterpart.[45] On the other hand, the Raman peak position after 30th charge cycle is well aligned with those in the 1st charge cycle at the threshold voltage of 3.0 V (Figure S16, Supporting Information). This observation further confirms that stable electrochemical interface can be achieved with chain-like Se, leading to improved electrochemical stability.

To obtain the phase evolution details of the Se@NPCFs during the second cycle, HRTEM images at different charge/discharge states were captured, along with their corresponding fast Fourier transform patterns (Figure 4c). The flat plateaus at 1.20 and 1.45 V agreed well with the peak positions in the CV curves, which corresponds to typical multi-step reactions. Before discharge, pristine Se confined in the micro/meso pores of the NPCFs displayed an amorphous structure. When discharging to 1.30 V, both HRTEM image and the FFT pattern indicate the formation of K_2Se_2 phase, as indicated by the lattice spacing matching well with the (002), (020), and (022) planes of K_2Se_2.[46] Particularly, the small K_2Se_2 phase clusters embedded in the fibers vanished under irradiation of electron beam. With the ongoing potassiation process in the Se@NPCFs electrode at 0.6 V, the metastable K_2Se_2 phase further evolved into a cubic K_2Se phase. The presence of lattice fringes of 2.1 and 1.9 Å, corresponding to the (222) and (400) planes, respectively, was the

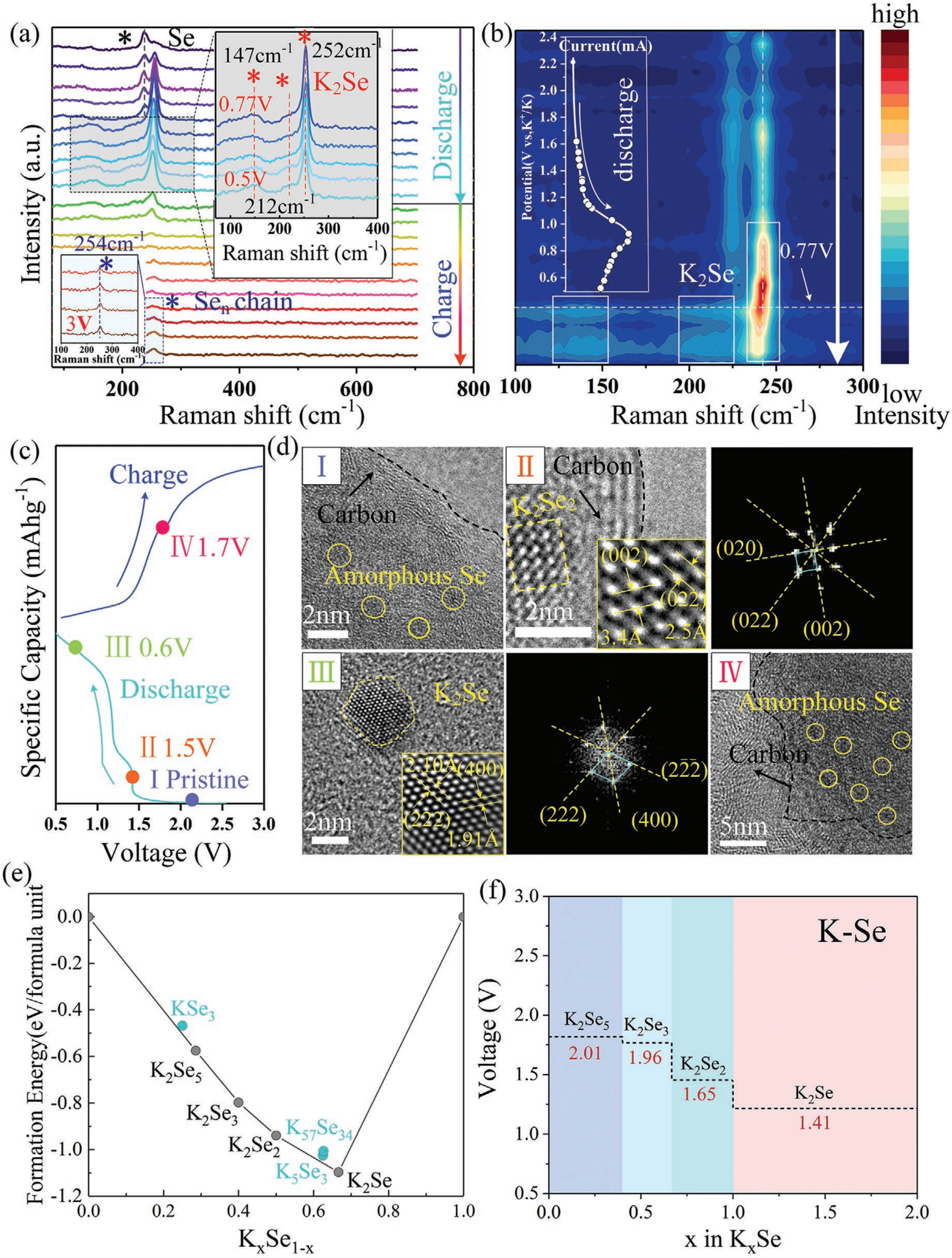

Figure 4. Mechanism of Se@NPCFs in the K–Se battery. a) In situ Raman analysis of the Se@NPCFs in the K–Se batteries at different discharge and charge stages in the first cycle. b) Contour plot of the Raman patterns of the Se@NPCFs during initial discharge process according to inset of (b): the selected points from CV profile at 0.2 mV s^{-1}. c,d) Ex situ HRTEM images of the Se@NPCFs electrode from the left discharge/charge curve at different states. e) Formation energies of existing potassiation selenides by theoretical calculations. f) Computed voltage curves for K_2Se_5, K_2Se_3, K_2Se_2, and K_2Se with reference to K^+/K.

evidence of the K_2Se phase.[10] Upon recharging to 3.0 V, the K_2Se was fully converted to amorphous Se, indicating the high reversibility of small-molecule Se in the Se@NPCFs during cycling. Based on the above results, a two-step potassiation mechanism is proposed for the Se@NPCFs electrode: small-molecule Se $\rightarrow$ K_2Se_2 $\rightarrow$ K_2Se, which is actually quite similar to Na–Se when it's confined in nanopores.[47] There are major differences in reaction path for Se depending on how it's incorporated into a host or if it's "free". It is also fundamentally different from the one-step conversion mechanism of Li–Se batteries previous reported.[9,48]

The conversion-based reaction mechanisms were further supported by density functional theory (DFT) calculations. The formation energies of potassium selenium compounds (Figure 4d) were calculated based on the K–Se binary phase diagram (Figure S17, Supporting Information) and existing databases. The stable structures exhibited on the convex tie-line, in an increasing order of K concentration, are K_2Se_5, K_2Se_3, K_2Se_2, and K_2Se. K_2Se has the lowest the formation energy, indicating its role as the most stable phase from a thermodynamic perspective. In addition, the average voltage profile was calculated between pairs of stable structures relative to metal K, which was depicted in Figure 4e. The theoretical potential of generating K_2Se and K_2Se_2 was about 1.41 and 1.65 V, respectively, which is ≈0.2 V higher than the experimental values. The small discrepancy in potential could be due to the overpotential caused by the electrode and electrolyte.[49] K_2Se_5 and K_2Se_3 phases were not reflected in the voltage plateau and above characterization results, demonstrating that the conversion reaction was favorably determined by kinetics rather than thermodynamics. Therefore, a multi-step all-solid-state reaction is proposed, where the Se chains are first transformed to intermediate K_2Se_2 before it is ultimately reduced to K_2Se.

More interestingly, we found the voltage profile of the Se@CFs differs substantially from that of Se@NPCFs, suggesting the existence of different reaction mechanisms. For the Se@CFs electrode (**Figure 5**a), a sloping voltage curve with two insignificant plateaus is the typical characteristic of solid solution reaction.[12,13] In contrast, the Se@NPCFs exhibits two flat plateaus with the second plateau significantly wider than the former one, which does not seem to be the same as the one-plateau discharge/charge behavior of typical cyclo-S_8.[41,50] Therefore, it is speculated that such an anomalous phenomenon is tied to the wetting nucleation process of two phases.[51] To clear this assumption, in-depth analysis was carried out. Fundamentally, the effect of NH_3 activation seems to be responsible for above phenomenon in view of the difference in the carbon matrix itself. From the non-local density functional theory (NLDFT) analysis (Figure 5b) that examined the micro/mesopore distribution of the as-synthesized samples, the CFs exhibit two broad peaks at about 1.4 and 2.5 nm. This is a good indication of the coexistence of micro/mesoporous nanostructure of the CFs, which also coincides well with the abovementioned analysis of adsorption–desorption curve. After the NH_3 activation, a large number of micropores with a scale of 0.5 nm was newly generated in the NPCFs. With such a variation in pore dimension, we might expect a vastly different molecular morphology of Se chains confined inside the carbon substrates. To shed light on the above analysis, theoretical calculations were employed to investigate the influence of pore structure on the selection pattern of the existence form about Se allotropes (Figure S18, Supporting Information). We find that the theoretical average of Se–Se distance will become longer as the increase of the length of Se allotropes (Figure 5c). This is in line with the EXAFs results that the Se–Se distance (2.02 Å) in the Se@NPCFs composite is shorter than that in the standard Se powder (2.09 Å) (Figure 5d). Basically, the main reason is that the Se powders comprising infinite helical Se chains were transformed into small-molecular selenium comprising short Se_n chains due to the size constrain during the process of infiltrating Se. Moreover, the optimized models of Se allotropes also show that the NPCFs micropores can filter out those longer-chain Se allotropes (Se_n, $3 \le n \le 8$) and are available for the accommodation of abundant short-chain Se_2 molecules that are smaller than 0.5 nm. Those melted long-chain Se_n (≥0.5 nm) can only disperse in the CFs with larger pore size (≥1.4 nm). The above conclusion was further evidenced by time-of-flight secondary ion mass spectrometry (TOF-SIMS) characterization to probe molecular information (Figure 5e). We only detected the signal of single-atom selenium as the main species for selenium, following by Se_2 and Se_3 with reduced intensity in the Se@NPCFs according to TOF-SIMS element mapping (Figure 5f). Generating the single-atom selenium needs to overcome high energy barrier, it can be deduced that the confined Se in the Se@NPCFs only exists in forms of abundant Se_2 and little Se_3 molecules. However, the strong signal of long Se_n (n = 4–8) chains molecules could be observed in the Se@CFs (Figure S19, Supporting Information). Given that the chain length of Se molecules is selectively limited by the pore size, it can be then concluded that the Se@NPCFs is more likely to undergo a two-phase conversion reaction without the formation of long-chain polyselenides. Based on the above discussion, the two flat plateaus of the Se@NPCFs can be interpreted as the solid-state phase transformation from short-chain Se_2 molecule to lower-order polyselenides K_2Se_2 and K_2Se, respectively. Indeed, this "all-solid-state" conversion reaction deviates from the conventional mechanism, where higher-order polyselenides (K_2Se_n, $n \ge 3$) is reduced as the side products of long-chain Se_n ($3 \le n \le 8$) inside the pores of CFs during the discharge process.[13] The reaction proceeds rather slow, resulting in sloped plateau that is similar to the observation in the Na–S battery system based on carbonate electrolyte.[52]

In addition, dQ/dV plots derived from the differentiation of the capacity–voltage curves at a low current density of 0.1 A g^{-1} was used to explain the two distinct conversion mechanisms between the Se@NPCFs and Se@CFs (Figure S20, Supporting Information). For the Se@CFs electrode, broadened peaks at 1.50 and 1.13 V represent the conversion from long-chain Se_n ($3 \le n \le 8$) to polyselenides (K_2Se_n, $3 \le n \le 8$), and the formation of K_2Se. This was confirmed by a simple investigation of the retrieved electrodes after discharging to 1.5 V. Surprisingly, the electrode turned blackish green in DME solvent while nothing has changed in the EC/DEC solvent (Figure 5g). These observations were in good agreement with the facts that long-chain K_2Se_n ($3 \le n \le 8$) are soluble in ethers, but not carbonates. In other words, the shuttle effect of polyselenides could be highly suppressed in the carbonate-based electrolyte.[53] Differing from the Se@CFs, the Se@NPCFs exhibit two individual sharp peaks that correspond to the formation of K_2Se_2

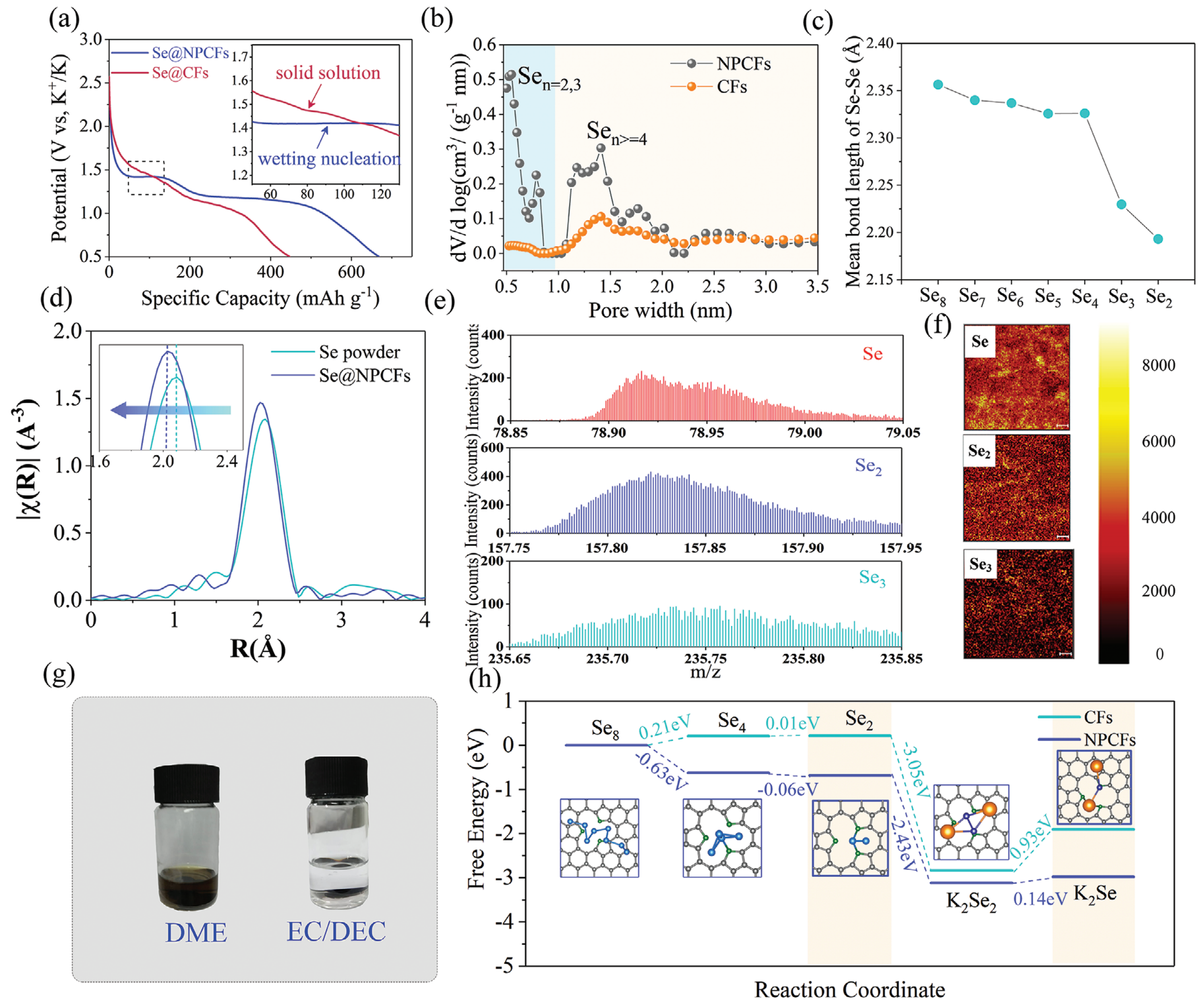

Figure 5. The investigation of different electrochemical behaviors for K–Se batteries. a) The comparison of third discharge curves between the Se@NPCFs and Se@CFs electrodes obtained at 0.1 A g^{-1}. b) The pore size distribution of CFs and NPCFs substrates. c) The theoretical average of Se–Se distance of Se allotropes from Se_2 to Se_8. d) EXAFS-FT in *R* space for Se@NPCFs electrodes and Se powder. e–f) TOF-SIMS mass spectrum of Se, Se_2^-, and Se_3^- in the Se@NPCFs composite and respective TOF-SIMS elements mapping. g) Solubility test of Se@CFs electrode in the ether (DME) and carbonate (EC/DEC) electrolyte when discharged to 1.5 V. h) Free energy profiles for different Se chains, K_2Se_2 and K_2Se on pure graphene and N-5 doped graphene respectively. Optimized structures for the intermediates (insets).

and K_2Se, indicating that the conversion takes place without the generation of polyselenides (K_2Se_n, $3 \le n \le 8$). Interestingly, the Se@NPCFs shows a lower polarization voltage (0.72 V) than that of the Se@CFs (0.93 V). This observation delineates the mechanistic difference between short-chain Se_2 and long-chain Se_n, where all-solid-state conversion of the Se@NPCFs entails faster reaction kinetics compared to the sluggish solid-solution reaction occurred in the Se@CFs. For the NPCFs, abundant mesopores can be expected from pore volume distribution (Figure S21, Supporting Information), meaning that Se_n ($3 \le n \le 8$) with moderate chain length may also be confined in it. However, this observation leads to a question regarding why Se@NPCFs and Se@CFs behave vastly different in carbonate-based electrolyte. To answer this, theoretical study was conducted. Herein, we take Se_8, Se_4 and Se_2 as examples. The free energy profile and optimized structures of the adsorbed intermediates are shown in Figure 5h. Obviously, the reaction step on the CFs substrate is uphill in free energy for all kinds of Se molecules regardless of chain length, but it demonstrates the opposite trend for the NPCFs substrate. It means that the deposition of Se_2 molecules on the NPCFs substrate is more favorable during the infiltration process due to the lower free energy, thus resulting in a higher mass loading of Se_2 on the NPCFs substrate.[54] In addition, the infiltration of Se_2 molecules into pores with sufficient N-doped sites is also more feasible. Moreover, the spontaneous exothermic reaction from Se molecules to K_2Se_2 and subsequently to K_2Se by endothermic reaction, regardless of Se chain form, signifies that the formation of K_2Se is the thermodynamic limiting step in the discharge process. This helps to explain why K_2Se_2 could be observed in the final products as a consequence of incomplete conversion as previously reported.[10] It is noteworthy that the transformation from K_2Se_2 to K_2Se on the CFs substrate requires 0.93 eV free energy, a much higher value above on the NPCFs (0.14 eV), which indicates that N-doping could facilitate the electrocatalytical reduction of Se_2 to K_2Se.

In summary, the rationally designed small-molecule Se embedded in free-standing peapod-like N-doped carbon nanofiber film electrode exhibits unprecedented K storage performance among all other reported Se-based cathodes. The synergistic effect of pore confinement and N-doping enables the outstanding performance of Se@NPCFs in the carbonate electrolyte. For instance, it delivers a capacity of 635 mAh g^{-1} over 50 cycles at 50 mA g^{-1} with a high Se utilization of 94.1%. Besides, it achieves a high reversible capacity of 367 mA h g^{-1} at a high current density of 0.5 A g^{-1} even after 1670 cycles, demonstrating excellent cycling stability. Moreover, the pouch cell with Se@NPCFs film exhibits superior mechanical flexibility, indicating its promising future in flexible K–Se batteries. More importantly, an "all-solid-state" two-phase reaction in Se@NPCFs was demonstrated to dominate the K–Se chemistry, opposed to the conventional single-step conversion mechanism involving dissolvable intermediate phases. The abundant short-chain Se_2 confined in the NPCFs could improve reactivity kinetics and eliminate the formation of high-order polyselenides (K_2Se_n, $3 \leq n \leq 8$), thus significantly enhancing the utilization of Se. Our work offers a practical strategy to optimize K–Se battery performance through structure engineering and manipulation of selenium chemistry.

Supporting Information

Supporting Information is available from the Wiley Online Library or from the author.

Acknowledgements

R.X. and Y.Y. contributed equally to this work. This work was supported by the National Key R&D Program of China (No. 2018YFB0905400), the National Natural Science Foundation of China (Nos. 52002083, 51925207, U1910210, 51872277, 51872283, and 2180527), the Fundamental Research Funds for the Central Universities (WK2060140026), the National Postdoctoral Program for Innovative Talents (BX20200318), the China Postdoctoral Science Foundation (2020M682031, 2020M672533), Dalian National Laboratory for Clean Energy (DNL) Cooperation Fund, CAS (DNL180310, DNL180308, DNL201912, DNL201915), Liaoning BaiQianWan Talents Program, LiaoNing Revitalization Talents Program (Grant XLYC1807153), DICP (DICP ZZBS201708, DICP ZZBS201802, and DICP I202032). The authors also thank the USTC Super Computing Center for the computational resources. Work at Argonne National Laboratory was supported by the U. S. Department of Energy (DOE), Office of Energy Efficiency and Renewable Energy, Vehicle Technologies Office under US-China clean energy program CERC-CVC2. Argonne National Laboratory is operated for DOE Office of Science by UChicago Argonne, LLC, under contract number DE-AC02-06CH11357.

Conflict of Interest

The authors declare no conflict of interest.

Keywords

potassium–selenium batteries, reaction mechanism, small-molecular Se

Received: June 7, 2020
Revised: October 9, 2020

---

[1] M. Li, J. Lu, X. Ji, Y. Li, Y. Shao, Z. Chen, C. Zhong, K. Amine, *Nat. Rev. Mater.* **2020**, *5*, 276.
[2] J. Lu, Z. Chen, F. Pan, Y. Cui, K. Amine, *Eletrochem. Energy Rev* **2018**, *1*, 35.
[3] B. Dunn, H. Kamath, J.-M. Tarascon, *Science* **2011**, *334*, 928.
[4] M. C. Lin, M. Gong, B. Lu, Y. Wu, D. Y. Wang, M. Guan, M. Angell, C. Chen, J. Yang, B. J. Hwang, H. Dai, *Nature* **2015**, *520*, 325.
[5] M. Li, J. Lu, Z. Chen, K. Amine, *Adv. Mater.* **2018**, *30*, 1800561.
[6] J. Chen, *Batteries Supercaps* **2019**, *2*, 401.
[7] A. Eftekhari, *Sustainable Energy Fuels* **2017**, *1*, 14.
[8] J. Ding, H. Zhou, H. Zhang, T. Stephenson, Z. Li, D. Karpuzov, D. Mitlin, *Energy Environ. Sci.* **2017**, *10*, 153.
[9] Y. Cui, A. Abouimrane, C. J. Sun, Y. Ren, K. Amine, *Chem. Commun.* **2014**, *50*, 5576.
[10] Y. J. Liu, Z. X. Tai, Q. Zhang, H. Q. Wang, W. K. Pang, H. K. Liu, K. Konstantinov, Z. P. Guo, *Nano Energy* **2017**, *35*, 36.
[11] M. Li, J. Lu, *Science* **2020**, *367*, 979.
[12] X. L. Huang, Q. J. Xu, W. Gao, T. T. Yang, R. M. Zhan, J. H. Deng, B. S. Guo, M. L. Tao, H. D. Liu, M. W. Xu, *J. Colloid Interface Sci.* **2019**, *539*, 326.
[13] X. Huang, W. Wang, J. Deng, W. Gao, D. Liu, Q. Ma, M. Xu, *Inorg. Chem.Front.* **2019**, *6*, 2118.
[14] W. Shin, J. Lu, X. Ji, *Carbon Energy* **2019**, *1*, 165.
[15] Y. Yao, M. L. Chen, R. Xu, S. F. Zeng, H. Yang, S. F. Ye, F. F. Liu, X. J. Wu, Y. Yu, *Adv. Mater.* **2018**, *30*, 1805234.
[16] R. Mo, D. Rooney, K. Sun, H. Y. Yang, *Nat. Commun.* **2017**, *8*, 13949.
[17] Y. Yuan, J. Lu, *Carbon Energy* **2019**, *1*, 8.
[18] Q. Sun, K. C. Lau, D. Geng, X. Meng, *Batteries Supercaps* **2018**, *1*, 39.
[19] Z. Li, J. T. Zhang, Y. M. Chen, J. Li, X. W. Lou, *Nat. Commun.* **2015**, *6*, 8850.
[20] B. Zhu, B. Cheng, L. Zhang, J. Yu, *Carbon Energy* **2019**, *1*, 32.
[21] X. Zhou, L. Chen, W. Zhang, J. Wang, Z. Liu, S. Zeng, R. Xu, Y. Wu, S. Ye, Y. Feng, X. Cheng, Z. Peng, X. Li, Y. Yu, *Nano Lett.* **2019**, *19*, 4965.
[22] Y. Yao, R. Xu, M. Chen, X. Cheng, S. Zeng, D. Li, X. Zhou, X. Wu, Y. Yu, *ACS Nano* **2019**, *13*, 4695.
[23] Y. Shi, G. Liu, R. Jin, H. Xu, Q. Wang, S. Gao, *Carbon Energy* **2019**, *1*, 253.
[24] Y. Sun, R. B. Sills, X. Hu, Z. W. Seh, X. Xiao, H. Xu, W. Luo, H. Jin, Y. Xin, T. Li, Z. Zhang, J. Zhou, W. Cai, Y. Huang, Y. Cui, *Nano Lett.* **2015**, *15*, 3899.
[25] Z. Li, B. Y. Guan, J. Zhang, X. W. Lou, *Joule* **2017**, *1*, 576.
[26] W. Yang, J. Zhou, S. Wang, W. Zhang, Z. Wang, F. Lv, K. Wang, Q. Sun, S. Guo, *Energy Environ. Sci.* **2019**, *12*, 1605.
[27] J. Yan, K. Dong, Y. Zhang, X. Wang, A. A. Aboalhassan, J. Yu, B. Ding, *Nat. Commun.* **2019**, *10*, 5584.
[28] B. Kalimuthu, K. Nallathamby, *ACS Appl. Mater. Interfaces* **2017**, *9*, 26756.
[29] H. Ye, Y.-X. Yin, S.-F. Zhang, Y.-G. Guo, *J. Mater. Chem. A* **2014**, *2*, 13293.
[30] Q. J. Xu, H. Liu, W. Y. Du, R. M. Zhan, L. Y. Hu, S. J. Bao, C. L. Dai, F. Liu, M. W. Xu, *Electrochim. Acta* **2018**, *276*, 21.
[31] Y. Yuan, G. Tan, J. Wen, J. Lu, L. Ma, C. Liu, X. Zuo, R. Shahbazian-Yassar, T. Wu, K. Amine, *Adv. Funct. Mater.* **2018**, *28*, 1706443.
[32] M. Marple, J. Badger, I. Hung, Z. Gan, K. Kovnir, S. Sen, *Angew. Chem., Int. Ed.* **2017**, *56*, 9777.

[33] Y. Xu, C. Zhang, M. Zhou, Q. Fu, C. Zhao, M. Wu, Y. Lei, *Nat. Commun.* **2018**, *9*, 1720.
[34] J. P. Song, L. Wu, W. D. Dong, C. F. Li, L. H. Chen, X. Dai, C. Li, H. Chen, W. Zou, W. B. Yu, Z. Y. Hu, J. Liu, H. E. Wang, Y. Li, B. L. Su, *Nanoscale* **2019**, *11*, 6970.
[35] L. N. Sha, P. Gao, X. C. Ren, Q. Q. Chi, Y. J. Chen, P. P. Yang, *Chem. - Eur. J.* **2018**, *24*, 2151.
[36] J. Ding, H. Zhou, H. L. Zhang, L. Y. Tong, D. Mitlin, *Adv. Energy Mater.* **2018**, *8*, 1701918.
[37] H. Tan, J. Tang, X. Zhou, D. Golberg, S. K. Bhatia, Y. Sugahara, Y. Yamauchi, *Chem. Commun.* **2018**, *54*, 9494.
[38] Z. Li, J. Zhang, Y. Lu, X. W. Lou, *Sci. Adv.* **2018**, *4*, eaat1687.
[39] C. Luo, Y. Xu, Y. Zhu, Y. Liu, S. Zheng, Y. Liu, A. Langrock, C. Wang, *ACS Nano* **2013**, *7*, 8003.
[40] S. X. C.-P. Yang, Y. a.-X. Yin, H. Ye, J. Zhang, Y. u.-G. Guo, *Angew. Chem., Int. Ed.* **2013**, *10*, 1002.
[41] X. Li, M. Banis, A. Lushington, X. Yang, Q. Sun, Y. Zhao, C. Liu, Q. Li, B. Wang, W. Xiao, C. Wang, M. Li, J. Liang, R. Li, Y. Hu, L. Goncharova, H. Zhang, T. K. Sham, X. Sun, *Nat. Commun.* **2018**, *9*, 4509.
[42] S. Xin, L. Gu, N. H. Zhao, Y. X. Yin, L. J. Zhou, Y. G. Guo, L. J. Wan, *J. Am. Chem. Soc.* **2012**, *134*, 18510.
[43] L. Syper, J. J. T. Mlochowski, *Terahedron* **1988**, *44*, 6119.
[44] D. Colombara, A. M. Gonçalves, A. Etcheberry, *Electrochem. Commun.* **2018**, *93*, 44.
[45] X. Zhou, P. Gao, S. Sun, D. Bao, Y. Wang, X. Li, T. Wu, Y. Chen, P. Yang, *Chem. Mater.* **2015**, *27*, 6730.
[46] W. Teichert, W. Klemm, *Z. Anorg. Allg. Chem.* **1939**, *243*, 86.
[47] F. A. Perras, S. Hwang, Y. Wang, E. C. Self, P. Liu, R. Biswas, S. Nagarajan, V. H. Pham, Y. Xu, J. A. Boscoboinik, D. Su, J. Nanda, M. Pruski, D. Mitlin, *Nano Lett.* **2020**, *20*, 918.
[48] C. P. Yang, Y. X. Yin, Y. G. Guo, *J. Phys. Chem. Lett.* **2015**, *6*, 256.
[49] M. Mortazavi, Q. Ye, N. Birbilis, N. V. Medhekar, *J. Power Sources* **2015**, *285*, 29.
[50] M. Helen, T. Diemant, S. Schindler, R. J. Behm, M. Danzer, U. Kaiser, M. Fichtner, M. A. Reddy, *ACS Omega* **2018**, *3*, 11290.
[51] C. Delmas, M. Maccario, L. Croguennec, F. L.e Cras, F. Weill, *Nat. Mater.* **2008**, *7*, 665.
[52] B. W. Zhang, T. Sheng, Y. D. Liu, Y. X. Wang, L. Zhang, W. H. Lai, L. Wang, J. Yang, Q. F. Gu, S. L. Chou, H. K. Liu, S. X. Dou, *Nat. Commun.* **2018**, *9*, 4082.
[53] P. Xiong, X. Han, X. Zhao, P. Bai, Y. Liu, J. Sun, Y. Xu, *ACS Nano* **2019**, *13*, 2536.
[54] Z. Du, X. Chen, W. Hu, C. Chuang, S. Xie, A. Hu, W. Yan, X. Kong, X. Wu, H. Ji, L. J. Wan, *J. Am. Chem. Soc.* **2019**, *141*, 3977.